Progress In Electromagnetics Research M, Vol. 77, 1–16, 2019

Microwave Time-Reversal Mirror for Imaging and Hyperthermia Treatment of Breast Tumors

Saptarshi Mukherjee*, Lalita Udpa, Satish Udpa, Edward J. Rothwell, and Yiming Deng

Abstract—A time reversal method is proposed for imaging and hyperthermia of tumors in breast tissues. Time reversal is based on the reciprocal nature of the electromagnetic scalar wave equation. Time reversed scattered electric fields recorded by the receiver antenna array are back-propagated in an FDTD assisted numerical model to focus back at tumor locations. The potential of this approach for thermal therapy applications is demonstrated by calculating specific absorption rates associated with the time-reversed electromagnetic fields. Simulation results elucidate the feasibility and robustness of the approach. A pulsed time domain measurement system is developed for conducting experiments to detect and measure heat absorbed by single and multiple tumors inside a simple breast phantom.

1. INTRODUCTION

Time reversal (TR) is based on the reciprocity property of the wave equation. Divergent waves emanating from a point source can be time-reversed and back-propagated in a non-dispersive medium to refocus back at the source. This property can be utilized for imaging since TR is equivalent to a matched filter approach, with a sharp peak produced at the source. TR can be used for imaging scatterers such as tumors since they behave as secondary sources. TR was introduced in 1992 by Fink et al. using ultrasonic waves for lithotripsy and transcranial therapy applications [1]. Later, in 2004, it was extended to electromagnetics [2], with recent applications spanning wireless communication, radar detection and nondestructive evaluation [3].

While X-ray mammography continues to be the most common breast cancer detection method [4], disadvantages such as risks associated with radiation exposure [5] and discomfort due to breast muscle compression [6] have motivated researchers to develop new modalities for breast cancer detection. With the advent of several imaging modalities for biomedical applications, there has been a huge thrust in using microwaves as a complimentary system for breast tumor screening and hyperthermia based treatment applications. Local hyperthermia has been shown to be effective in several clinical studies, including breast cancer as an adjuvant method to radiation and chemotherapy [7]. While some narrow band signal schemes have been used for hyperthermia treatment applications [8], ultra-wideband (UWB) systems offer several advantages such as tighter focal spots and reduced hot spot anomalies due to its lower sidelobe peaks [9]. A comparison of performance between UWB and narrow band systems of hyperthermia for breast cancer treatment has been reported in [10]. While a lot of research has been focused on using beamforming imaging techniques [11–13], TR has unique advantages over the conventional reconstruction algorithms. It is non-iterative and has super-resolution [14] and selective focusing [15] capabilities. Other new microwave inversion methods such as the direct sampling method and orthogonality sampling method are being developed for near field imaging

Received 20 September 2018, Accepted 25 November 2018, Scheduled 8 December 2018
* Corresponding author: Saptarshi Mukherjee (mukher40@msu.edu).
The authors are with the Department of Electrical and Computer Engineering, Michigan State University, East Lansing, Michigan 48824, USA.

applications [16]. However, constraints such as requirement of weakly contrasting, bounded target and circular measurements enclosing the target and diffraction limited resolution limit their application [17]. The biggest advantage of time reversal imaging (TRI) is the fact that a physical TRI system has the potential to focus the non-ionizing microwaves inside the tumor region. The focused electromagnetic fields preferentially heat the tumor, thus opening up the scope towards microwave-induced thermal therapy applications [18, 19]. While there are several other microwave imaging modalities currently being investigated by other researchers for imaging breast tissues, they would require two separate modules for imaging and focusing such as a phased array approach [20] for hyperthermia applications. The novelty of this approach and the benefit of TR is that it can physically focus the non-ionizing microwaves inside the tumor, leading to imaging as well as preferential heating of the tumor. This opens up the scope of using the same TRI hardware system for imaging and thermal therapy applications, as has been done for transcranial therapy by Fink et al. using ultrasonic waves [21].

A novel TRI system is proposed in this paper for imaging and hyperthermia of breast tumors. The challenges associated with developing a robust TRI framework in the context of breast tissue imaging are discussed. The first part of the paper introduces TR theory, an algorithm for its implementation and an imaging assisted hyperthermia treatment. The second part of the paper deals with TR simulations and parametric studies associated with a numerical model of a coronal section of a human breast. The final part of the paper deals with experimental studies conducted for imaging and determining energy absorption rates for both single and multiple tumors placed in a simple breast phantom. One of the novelties of this research is the optimal detection and energy absorption inside breast tumors without knowledge of the breast heterogeneity. Additionally, while there has been very few papers showing active TR microwave imaging experimental results for breast tumor detection [8], this paper is the first to introduce a pulsed time domain experimental system for active microwave imaging of fatty breast tissues. The efficiency of the overall algorithm and experimental system is demonstrated, laying the foundation for potential therapeutic applications for breast cancer.

2. THEORETICAL METHOD FOR TRI

The theory of TR relies on the time-symmetric nature of the electromagnetic wave equation in a lossless medium, as given by [2]

$$\left(\nabla^2 - \frac{n^2(r)}{c^2}\frac{\partial^2}{\partial t^2}\right)\varphi(r,t) = 0. \tag{1}$$

where c is the speed of light in free space, and n is the refractive index. The equation is satisfied by a causal, diverging solution $\varphi(r,t)$ along with an anti-causal, converging solution $\varphi(r,-t)$. Thus, diverging waves emanating from a source can be reversed in time and back-propagated in space to focus at the source. The theory of TR has been well established over the past two decades [22]. A review of the evolution of electromagnetic TR theory and techniques and its difference from phase conjugation is discussed in [23, 24].

2.1. TR Algorithm

The theory of TR can be extended towards imaging tumors in multi-layered breast tissues. Numerical back-propagation of perturbation fields due to tumors in a healthy breast model focuses fields at the tumor location since the perturbation field can be thought of as the field produced by a source occupying the region of the tumor. The proposed approach as outlined in Fig. 1, uses a non-iterative, direct imaging approach, rather than a regularization based iterative approach, leading to reduced computational time. A short pulse is transmitted from an antenna and propagates into the region of interest, i.e., the breast tissues. Scattered signals due to malignant and healthy breast tissues are measured by the receivers and subtracted to obtain the perturbation signal. Next, the perturbation signal waveform is time reversed and backpropagated in a healthy breast model. Visualization of the back-propagated wave shows the fields initially converging, focusing near the tumor region, and then diverging. The time integrated energy of the TR fields provides a localized image of the tumor. Prior research on TR simulations for breast imaging assumed perfect knowledge of breast properties, which is unrealistic in practical

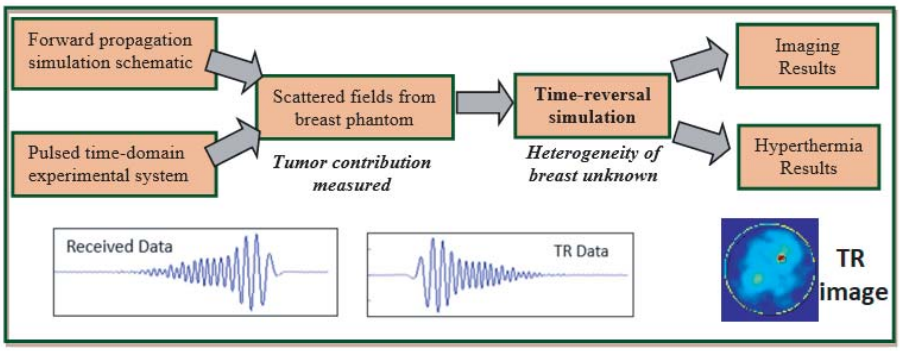

Figure 1. Proposed approach of TR for imaging and hyperthermia.

biomedical applications. In this paper, the robustness of the TR algorithm is demonstrated without considering the medium heterogeneity, and knowing only the nominal breast properties.

2.2. Hyperthermia Study via TR

Hyperthermia is an effective, thermal therapy technique used to elevate cell temperatures and thus induce cytotoxic effects in tissues, leading to cell damage and increased vulnerability to radiation and toxins [25]. The objective of this treatment is to elevate the temperature of tumor cells to $\sim$ 42°C–43°C, while maintaining the temperature of the rest of the tissues below 42°C [10]. Recent research on the development of cheap and compact RF circuits for TR of UWB pulses with nanosecond temporal durations has demonstrated the possibility of a physical TRI system [26]. One of the biggest advantages is TR, which lies in the fact that a physical TR system can focus the non-ionizing microwaves inside the tumor, leading to preferential heating of the tumor. This opens up the scope towards hyperthermia treatment applications. The specific absorption rate (SAR) evaluates the heat generated in the tissue by the electrical field, as given by

$$\mathrm{SAR} = \frac{1}{2}\int \frac{\sigma(r)|E(r)^2|}{\rho(r)}dr, \tag{2}$$

where σ and ρ are the tissue electrical conductivity and density respectively, and $|E(r)|$ is the magnitude of electric field in the breast tissues. This paper investigates the feasibility of utilizing this approach for measuring heat generated in the tumor for potential therapy, in complement with imaging applications.

2.3. Quantitative Metrics

Several quantitative metrics can be utilized as performance indicators of the method. The mean electric energy (mE) and mean SAR ratio (mSAR) are introduced to quantify the relative absorbed energy in the tumor. They serve as quantitative comparisons for detection capability of the focused field images and are given by

$$\mathrm{mE} = \frac{\frac{1}{X_t}\sum^{A_t} E(x,y)}{\frac{1}{X_{nt}}\sum^{A_{nt}} E(x,y)}, \quad \mathrm{mSAR} = \frac{\frac{1}{X_t}\sum^{A_t} \mathrm{SAR}(x,y)}{\frac{1}{X_{nt}}\sum^{A_{nt}} \mathrm{SAR}(x,y)}, \tag{3}$$

where X_t is the total number of pixels, A_t the area of the tumor region, X_{nt} the number of pixels, and A_{nt} the area of the rest of the breast region. The numerator involves the total number of pixels for the imaging domain within the tumor, while the denominator involves the total number of pixels for the imaging domain within the breast and skin region. Thus mE and mSAR indicate the ratio of the average TR energy and heat generated on the tumor with respect to the average TR energy and heat generated on the breast tissues, including the skin layer.

3. NUMERICAL STUDIES

As described earlier, the proposed TR algorithm uses a non-iterative approach, thus reducing the computational time. The numerical studies are performed using an in house developed tool based on finite difference time domain (FDTD) 2D transverse magnetic to the z direction [27], with perfectly matched layers as boundaries. The governing equations are explained in [3]. Breast tissues are lossy and inhomogeneous. The TR electric field FDTD equation for a lossy medium is given by

$$E_z^{n+1}(i,j) = \frac{1-\frac{\sigma\Delta t}{2\varepsilon}}{1+\frac{\sigma\Delta t}{2\varepsilon}}E_z^n(i,j) - \frac{1}{1+\frac{\sigma\Delta t}{2\varepsilon}}\frac{\Delta t}{\varepsilon\Delta x}\Big(H_y^{n+1/2}(i+1/2,j) - H_y^{n-1/2}(i-1/2,j) - H_x^{n+1/2}(i,j+1/2) + H_x^{n-1/2}(i,j-1/2)\Big) \quad (4)$$

where ε and σ are the material permittivity and conductivity respectively, and Δt and Δx are the FDTD time steps and cell size, respectively. The FDTD grid size is chosen fine enough ($\lambda/50 = 3\,\text{mm}$) such that the area of the tumor lies almost perfectly in a square pixel grid. Although the classical theory of TR is based on a lossless medium as shown in Eq. (1), it can be extended to compensate for attenuation in a lossy medium by changing the sign of conductivity in Eq. (4). The Debye's loss constant (α) is given by [28]

$$\alpha = \omega\sqrt{\frac{\mu_0\varepsilon'}{2}\sqrt{1+\frac{\sigma}{(\omega\varepsilon')^2}}-1} \quad (5)$$

The attenuation constant is inversely related to the penetration depth (δ) and thus gives a measure of the primary amount of electromagnetic fields interacting with the tissues. It is worth mentioning that the compensation is valid only when α is sufficiently smaller than the wavelength, that is, $\alpha \ll c\omega^{-1} = \lambda$. The receiver and transmitter antennas are modeled as point entities. The scattered field data were obtained for 80 equally spaced receiving antenna positions. The input source is chosen as a short modulated Gaussian pulse with a center frequency of 2 GHz and pulse width of 120 picoseconds, giving a bandwidth of 5.5 GHz. The simulation schematic along with the antenna array system is shown in Fig. 2.

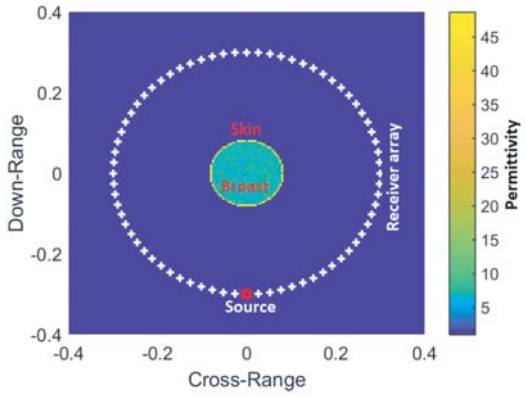

Figure 2. Simulation schematic with breast and antenna positions.

3.1. Breast Phantom Model

The breast phantom model chosen for simulation is a two-dimensional coronal section of radius 8 cm, with the dimensions and dielectric properties matching a realistic breast slice obtained from the Voxel CAD model of the University of Wisconsin Numerical Breast Phantom Repository coronal section for

a fatty tissue [29]. The advantage of the chosen model is that all features such as tumor size, spacing and dielectric properties are parametrically defined and are used to obtain a parametric analysis to determine the robustness and limits of the TRI algorithm. The tumor, of radius varying from 6 mm to 1 cm, is placed at different locations inside the breast phantom. The breast is assumed to comprise mostly fatty tissues with $\varepsilon_r = 7$ and $\sigma = 0.012\,\mathrm{S/m}$ at 6 GHz with 20% tissue variance and a skin layer of thickness 2 mm with $\varepsilon_r = 48.6$ and $\sigma = 0.078\,\mathrm{S/m}$ at 6 GHz, while the tumor's dielectric properties are assumed to be $\varepsilon_r = 50$ and $\sigma = 0.086\,\mathrm{S/m}$ at 6 GHz. The dielectric properties of the malignant and non-malignant breast tissues are chosen from [28].

3.2. Simulation Analysis

Simulation studies replicating the desired experiments are conducted to determine the feasibility of the algorithm. Parametric studies as well as specific simulation cases are considered to determine the robustness and limits of the TRI algorithm with respect to medium inhomogeneities, electrical property contrast between breast and tumor tissues, multiple tumors and the bandwidth of the input pulse. A default tumor radius of 4 mm is chosen for the parametric studies. The quantitative metrics used in the studies are given by mE and mSAR. Four different sets of parameters considered are outlined in Table 1, and corresponding results are presented in the following section.

Table 1. Simulation cases.

Parameters	Details	Cases	Threshold
Heterogeneity	$\varepsilon_r\sigma$ variance	20%, 40%, 80%	75%
	Scatterer	1, 2, unknown	-
Tumor spacing	2 tumors	1 cm, 4 cm, 2.8 cm	1.5 cm
	3 tumors	2.5 cm, 5 cm	-
Material contrast	1–10	-	2.25
Bandwidth	2–48 GHz	-	3 GHz

3.2.1. Tissue Heterogeneity

It is difficult to estimate the heterogeneity of dielectric properties of breast tissues due to multiple reasons, such as water and fat concentrations that vary with each individual. Tissue heterogeneity can be attributed due to variations of nominal dielectric properties of tissues as well as presence of non-tumorous scatterers.

Although the expected variations have been reported to be $\sim$ 10–20% in literature [30], variations of up to 80% of the nominal values ($\varepsilon_r = 7$, $\sigma = 7\,\mathrm{S/m}$) are considered here. The variation $(\varepsilon_r^v, \sigma^v)$ is introduced as a uniformly distributed random variable around the nominal dielectric properties, as given by $\varepsilon_r^v \sim U(\varepsilon_r(1+\psi), \varepsilon_r(1-\psi))$; $0 \leq \psi \leq 1$. Here U denotes uniform distribution, and ψ is the variance. TR back-propagation simulations are performed, with only the nominal values of the electrical properties of breast tissues known. The behavior of TRI is similar to that of a matched filter, with the TR fields producing a sharp peak where the fields focus. In the absence of medium heterogeneity, the TR signal (s_{TR}) for N receivers with an impulse input is given by

$$s_{\mathrm{TR}}(t) = \sum_{n=1}^{N} h_n(t) * h_n(-t), \tag{6}$$

where $h_n(t)$ and $h_n(-t)$ are the forward and backward impulse response functions. When a medium heterogeneity $\delta_n(t)$ is considered, s_{TR} is given by

$$s_{\mathrm{TR}}(t) = \sum_{n=1}^{N} (h_n(t) + \delta_n(t)) * h_n(-t). \tag{7}$$

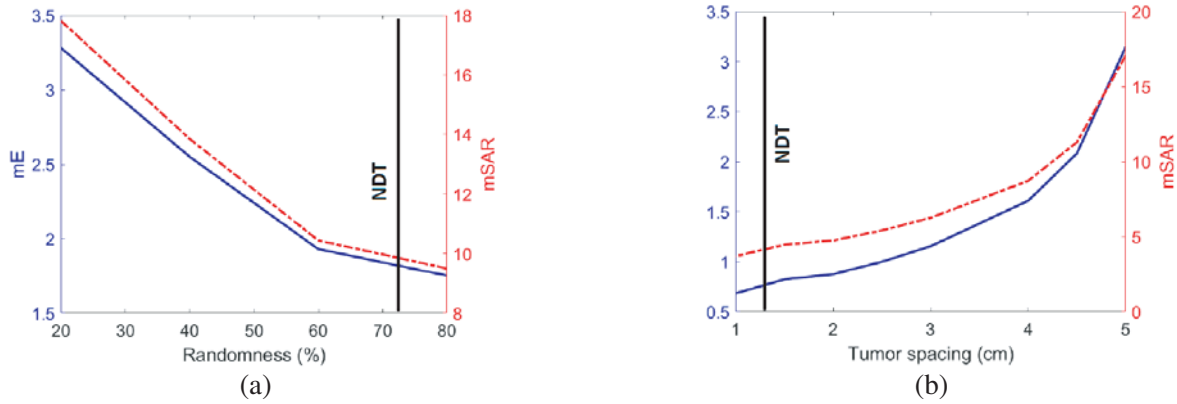

Figure 3. Results of parametric studies: mE and mSAR with (a) tissue dielectric variance, (b) tumor spacing (NDT: non detectable tumor).

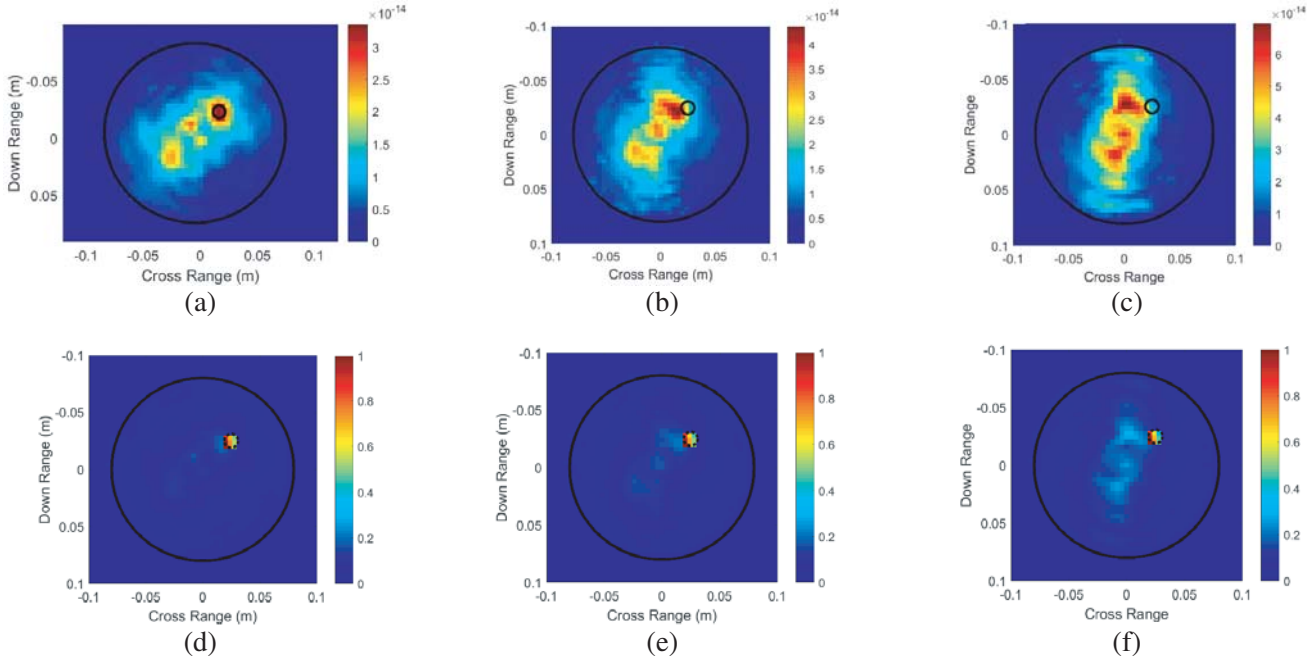

Figure 4. Case I — TR imaging results for varying tissue heterogeneity. (a), (d): 20% heterogeneity; (b), (e): 40% heterogeneity; (c), (f): 80% heterogeneity. (a) Energy (mE = 3.5), (b) Energy (mE = 2.5), (c) Energy (mE = 1.8), (d) SAR (mSAR = 18), (e) SAR (mSAR = 13), (f) SAR (mSAR = 9.5).

Low level dielectric variance is not matched with the nominal medium response and hence does not dramatically affect the time reversed signal. Increased dielectric variance leads to an increase in forward and backward impulse response function mismatch, thus leading to lower mE and mSAR. Fig. 3(a) shows the parametric variation of mE and mSAR with variation of tissue. The threshold of tissue variation is estimated around 70%, above which $\delta_n \gg h_n$ and thus the tumor is not detected in the energy image. Three specific cases are simulated and shown for tissue variance of 20, 40 and 80%. As shown in Figs. 4(a), (b) and (c), the TR field results show that the dielectric variance of the medium is mismatched with the nominal medium impulse response. Although the imaging quality is not severely hampered by marginal dielectric variance, the tumor is barely detected for 80% variation due to the huge mismatch between the forward and backward impulse response functions. The SAR images, shown in Figs. 4(d), (e) and (f), show a similar trend in absorption with the tumors absorbing

higher energy than the surrounding tissues, with approximately 30% higher absorption for 80% tissue variation. Equation (2) takes into account the effect of closer tissues to antennas. Thus although there is a strong reflection at tissues closer to the antennas, due to the medium mismatch, the time reversed EM fields back-propagate to focus at the tumor due to TR's matched filter nature described above. Thus there is not a considerable increase of SAR near tissues closer to the antennas.

The presence of non-tumorous scatterers in breast tissues may also lead to medium heterogeneity. The robustness of the TRI algorithm to detect a tumor in the presence of elliptical single and multiple scatterers with $\varepsilon_r = 4$ and $\sigma = 0.012\,\mathrm{S/m}$ with a 20% tissue variance is investigated. Although the scattered fields consist of scatterer and tumor contributions, a significant portion of the TR field still focuses on the tumor, and thus detection is possible for single and multiple scatterers, as shown in Figs. 5(a) and 5(b), when the scatterer property is known in the TRI model. If the scatterer size is much larger than the tumor, higher TR energy is focused around it, rather than around the tumor, as observed in Figs. 5(a) and (c). Some additional artifacts are observed between the tumor and the scatterers due to the cross coupling between them. For two well resolved scatterers, the TR signals correspond to a linear combination of non-null orthogonal eigenvectors. However, since the inhomogeneities and tumor are not point scatterers and are not well separated, the corresponding eigenvectors are non orthogonal, resulting in poor image quality. However, when the scatterer property is unknown, the tumor cannot be detected, as seen in Fig. 5(c). The focusing ability of the TR method, which is due to its matched filter property, is lost since the forward and backward impulse response functions, as defined in Eq. (7), are different. Sophisticated signal processing algorithms are required in this case to extract the tumor contribution from the scattered fields. These algorithms employ selective focusing methods such as decomposition of the time reversal operator method [31] to extract the eigenvalue corresponding to the tumor and steer its eigenvector towards the tumors. Additional clutter, breast inhomogeneities and skin-wall interaction can be eliminated by employing a time of arrival approach to determine the time duration when the wave is localized inside the breast region. These are currently being investigated and not addressed in this research. The TR SAR images (Figs. 5(d), (e), (f)) are much more focused

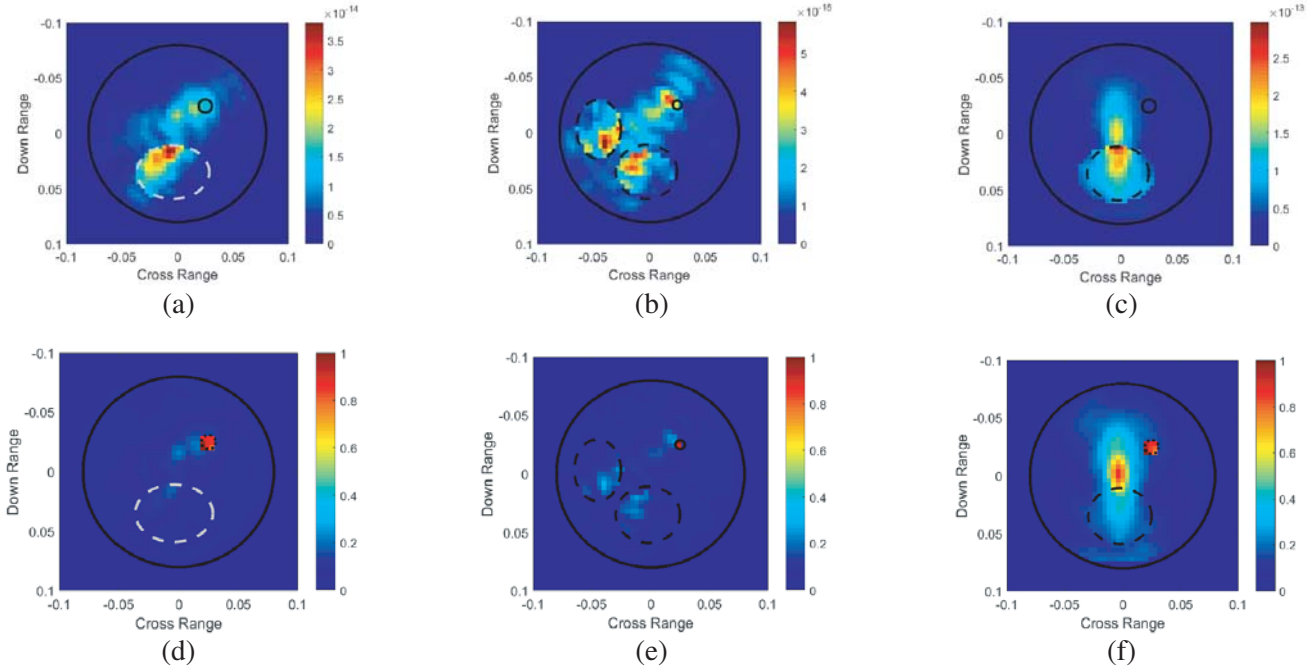

Figure 5. Case II — TR imaging results in presence of inhomogeneity. (a), (d): 1 ellipse major axis 6 cm; (b), (e): 2 ellipsis major axis 5 cm; (c), (f): unknown scatterer (ellipse major axis 6 cm). (a) Energy (mE = 3.2), (b) Energy (mE = 3.4), (c) Energy (mE = 0.5), (d) SAR (mSAR = 12), (e) SAR (mSAR = 15), (f) SAR (mSAR = 8).

on the tumor, since the conductivity of the tumor is larger than the surrounding fatty tissues and other scatterers.

3.2.2. Tumor Spacing

Incidence of multiple tumors in the breast in the form of multi-focal or multi-centric disease have been reported in the literature to range between 6 and 60% [32]. Multi-centric disease has been reported to occur in breast cancer cases, where multiple lobules or ducts of size around 2 cm with minimum spacing around 0.5 cm may develop in different breast segments [33]. TR has the capability of imaging multiple targets, as long as the separation between them is of the order of a wavelength. This is challenging for imaging breast tissues, as tumors might be near each other or to the skin interface. The feasibility of the TRI algorithm for detection of multiple closely spaced tumors is studied in this section. Fig. 3(b) shows the parametric variation of mE and mSAR with the spacing between two tumors, with the minimum spacing, below which the tumor is not detected in the energy image estimated as 1.5 cm, which is approximately half of the down range resolution. This is due to the multi-path scattering from the tumors that increase the TRM aperture and hence leads to higher resolution. An increase in spacing between two tumors leads to reduced cross-coupling and hence better imaging quality and higher mE and mSAR. Three specific cases are studied for imaging two and three tumors. For two tumors closely spaced with a gap of 2.8 cm, as shown in Fig. 6(a), the back-propagated wave focuses equally at the two tumor locations, showing two sharp peaks at the respective tumor locations. However, when the gap is 1.4 cm (lower than the threshold value obtained from Fig. 3(b)), the strong cross coupling between them and the limits of diffraction resolution are responsible for producing an extended focal spot, as shown in Fig. 6(b). A third case is considered with 2 tumors of radius 0.6 cm named as T1 and T2 and a bigger tumor of radius 1.2 cm named T3, placed inside the breast. The gap between T1 and T3 is 5 cm, while the gap between T2 and T3 is 8 cm, with their exact locations shown in Fig. 6(c). It is seen that the detection capability of cross-range separated tumors is better than for down-range separated tumors. The TR wave focuses more on T3 since it is larger than the other tumors. Additionally, cross-

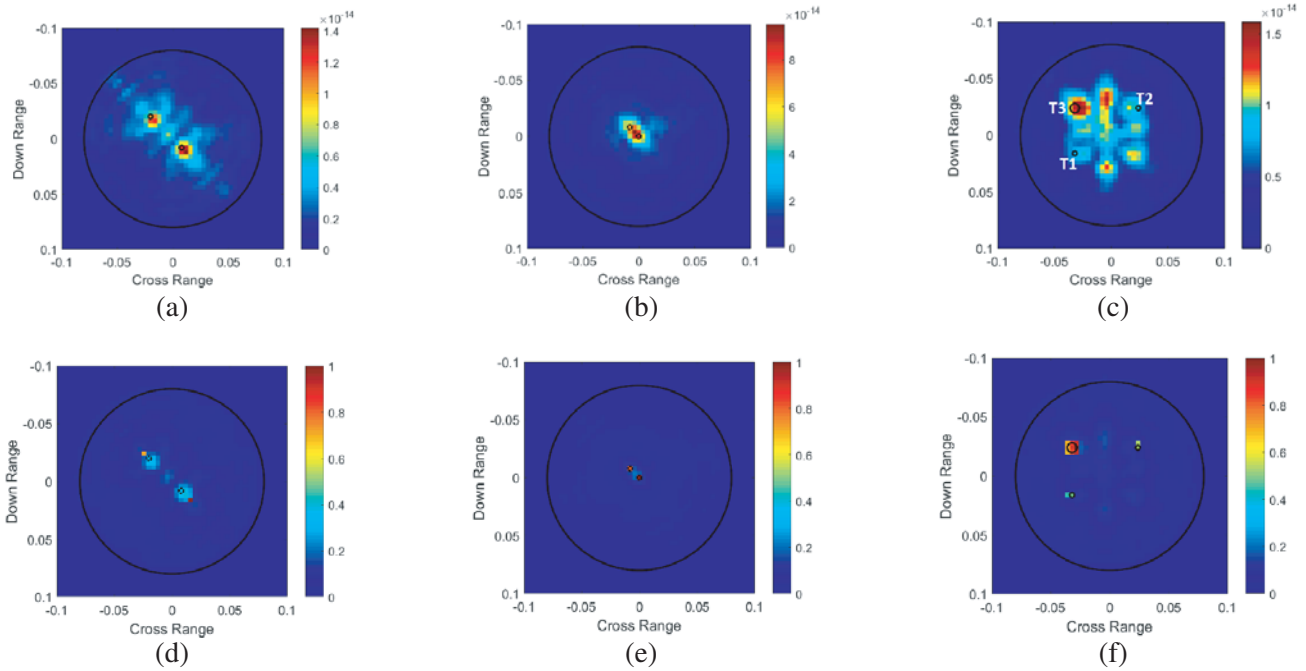

Figure 6. Case II — TR imaging results for varying gap between tumors. (a), (d): 2 tumors gap = 2.8 cm; (b), (e): 2 tumors gap = 1.4 cm; (c), (f): 3 tumors gap = 5 cm and 8 cm. (a) Energy (mE = 1), (b) Energy (mE = 0.6), (c) Energy (mE = 1), (d) SAR (mSAR = 7), (e) SAR (mSAR = 5.5), (f) SAR (mSAR = 9).

coupling between the tumors leads to artifacts as shown in Fig. 6(c). The SAR image, seen in Fig. 6(d), shows a similar trend in absorption with the tumors absorbing higher energy than the surrounding tissues. Figs. 6(e) and 6(f) show that for two closely spaced tumors as well as a tumor, breast fatty tissues surrounding the tumors absorb a considerable amount of energy, which is undesirable for thermal therapy.

3.2.3. Material Contrast Ratio

The dielectric properties of the non-malignant breast tissues vary significantly with varying fat and water concentrations. In general, fibroglandular tissues have much higher ε_r, σ than fatty tissues, and their dielectric properties may be closer to that of malignant tissues. Tumor detection might be difficult in such cases due to less dielectric contrast. The capability of TR to detect tumors for different dielectric properties of breast tissues is investigated. The dielectric constant and conductivity ratio between the tumor and surrounding breast tissues is defined as contrast ratio. Simulations are conducted by varying the contrast ratio from 1 to 10 in order to determine the robustness of TRI. Fig. 7(a) shows the parametric variation of mE and mSAR with the contrast ratio between breast and tumor tissues. The threshold of the contrast ratio, below which the tumor is not detected in the energy image, is estimated to be 2.25.

The effect of high water content and implicit conductivity of the tumor tissues on the TR algorithm is also studied. The performance of the algorithm was evaluated by comparing a tumor with a high water content ($\varepsilon_r = 50$, $\sigma = 5\,\mathrm{S/m}$) and a tumor with a low water content ($\varepsilon_r = 50$, $\sigma = 0.086\,\mathrm{S/m}$) and shown in Figs. 8(a), (c) and Figs. 8(b), (d). The TR energies show comparable imaging quality, while the SAR images show much higher absorption around the tumor with higher conductivity. The

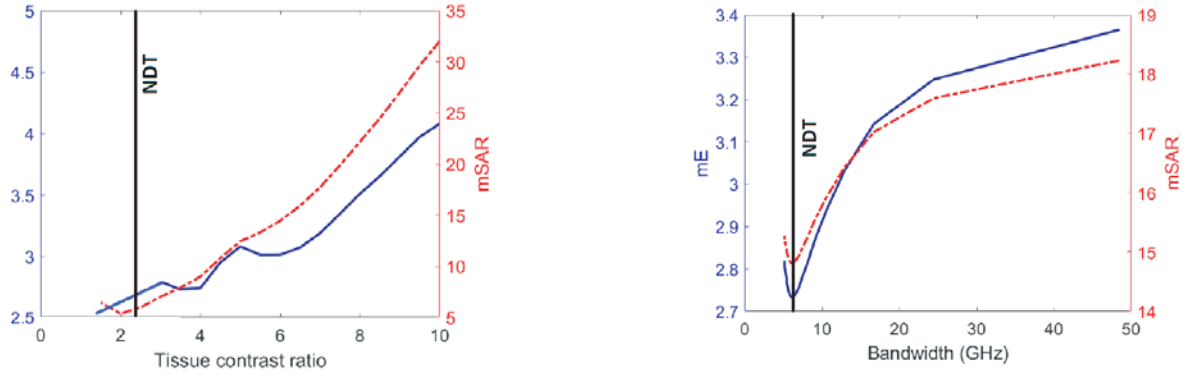

Figure 7. Results of parametric studies: mE and mSAR with (a) tissue contrast, (b) input pulse bandwidth.

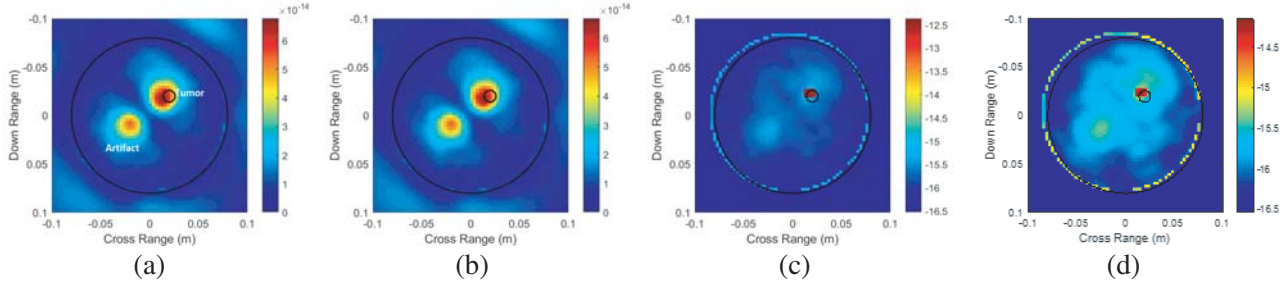

Figure 8. Case III — TR imaging results for varying conductivity of tumor. (a), (c): $\varepsilon_r = 50$, $\sigma = 5\,\mathrm{S/m}$; (b), (d): $\varepsilon_r = 50$, $\sigma = 0.086\,\mathrm{S/m}$. (a) Energy (mE = 9), (b) Energy (mE = 9.2), (c) SAR (mSAR = 20), (d) SAR (mSAR = 2).

high dielectric constant of the tumor tissues ($\varepsilon_r = 50$) results in a high reflection coefficient ($\tau = 0.75$). Thus most of the fields are scattered from the tumor outer boundary, with no significant penetration that would interact with the tumor. Hence the imaging quality is not degraded due to an increase in tumor conductivity. However, an increased conductivity results in higher energy absorption by the tumor region in accordance with (2). While mE is almost constant and decreases slightly varying values of conductivity, mSAR increases with increasing conductivity due to more energy absorbed in tumor with respect to surrounding tissues.

3.2.4. Bandwidth

The imaging quality of TRI also depends heavily on the input pulse width, since TR involves focusing both in space and time. Fig. 7(b) shows the parametric variation of mE and mSAR with respect to the pulse bandwidth. A pulse with a shorter width and hence a bigger bandwidth leads to better range resolution and thus leads to enhanced imaging quality. The relationship between the range resolution (S_r) and pulse width (τ) is given by $S_r \geq \frac{c}{2\tau}$. Thus, an increase in bandwidth leads to increased mE and mSAR respectively, as seen in Fig. 7(b). As mentioned before, the conductivity of breast tissues is fixed at 0.012 S/m throughout the bandwidth. However if frequency dispersiveness is considered, the conductivity of breast tissues is expected to rise with an increase of frequency, which should limit the penetration of high frequency signals leading to a decrease of mE and mSAR at high frequencies. The bandwidth threshold, below which the tumor is not detected in the energy image is estimated to be 3 GHz. Other parameters that affect the imaging quality are tumor size, receiver array and noise. These are discussed in [34, 35].

3.2.5. Effect of Noise

As mentioned before, the perturbation fields due to tumor are retrieved by subtracting scattered fields from healthy and non-healthy breast tissues. The tumor response is typically much less (order of 2) than the response due to the total fields, as shown in Fig. 9(a). However, the effect of the tumor would still add a significant contribution due to the inherent matched filter capability of the TR approach. The back-propagated signal in presence of measurement additive noise $\delta_n(t)$ is given by $h_r(-t)+\delta_n n(t)$. Thus the time reversed signal without knowledge of medium variance can be represented as

$$\begin{aligned} s_{\mathrm{TR}}(t) &= \sum_{n=1}^{N} (h_n(t) + \delta_n(t)) * (h_n(-t) + n(t)) \\ s_{\mathrm{TR}}(t) &= \sum_{n=1}^{N} (h_n(t) * h_n(-t) + h_n(t) * n(-t) + \delta_n(t) * h_n(-t)) + \delta_n(t) * n(t)) \end{aligned} \tag{8}$$

Low level dielectric variance and low level measurement noise are not matched with the nominal medium response. Thus the first convolution term of Eq. (8) constructively interferes, while the other convolution terms are mismatched, and hence does not dramatically affect the time reversed signal. As long as the

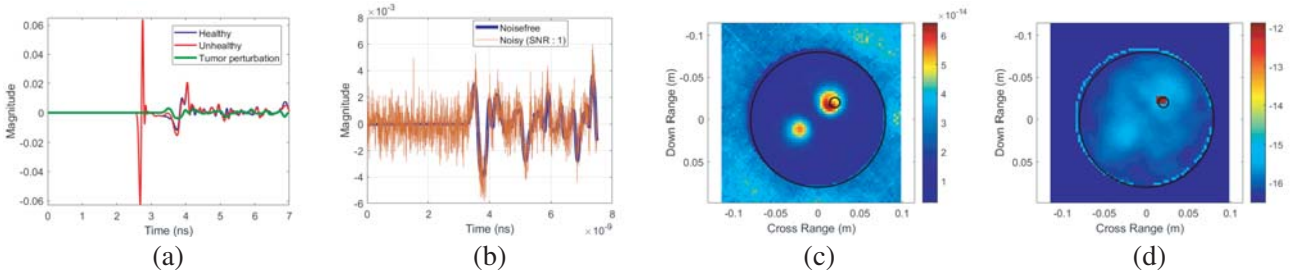

Figure 9. Case IV — (a) Scattered fields and tumor contribution for one receiver element, (b) addition of noise (SNR = 1) to tumor signals, (c), (d): TR results for noisy signals. (c) Energy (mE = 4), (d) SAR (mSAR = 8.9).

phase difference between successive receiver array elements is unhampered, TR focusing can be achieved effectively, even in the presence of noise and unknown medium variations. Additive white Gaussian noise with an SNR of 2 dB is added individually to all receiver signals after measuring the power of the signals. A typical noise-added tumor signal is shown in Fig. 9(b). As long as the phase difference between successive receiver array elements is unhampered, TR focusing can be achieved effectively, as seen in Figs. 9(c), (d).

4. EXPERIMENTAL STUDIES

Experimental validation of the TRI approach was undertaken using a microwave pulsed time-domain system.

4.1. Experiment Details

The experimental system is depicted in Fig. 10(a). A wooden arch range of diameter 20 cm with a circular platform was constructed to position the sample and antennas. Based on the properties of time reversal and its imaging applications, an antipodal Vivaldi antenna and a monopole antenna were proposed for the transmitter and receiver designs, respectively [36]. The antennas were designed to have a UWB performance, operating between 3 to 10 GHz. Although the transmitting antenna has a beamwidth narrow enough to illuminate the breast tissues effectively, the beam cannot be too focused, since TR theory is based on waves diverging outwards from a point source. In contrast, the receiving antennas have omnidirectional radiation patterns, since they behave in radiation mode as point sources of the TR back-propagation model. The microwaves need to be sufficiently well focused in the coronal plane, with less scattering from above and below the plane, such as reflections from the chest wall. In addition, since a 2D imaging algorithm is used, the cross-polarized electric field components from the transmitting antenna are lost, leading to a degradation of the overall imaging quality of the 2-D algorithm. These undesired field components are minimized by maintaining the cross polarization of the antenna as low as possible. Simulation and measurement results demonstrate the efficiency of the antennas for a time reversal mirror. The receiver is moved, keeping the transmitter fixed in order to emulate the antenna array system. Similar to simulations, the scattered field data were obtained for 20 equally spaced receiving antenna positions. A pseudo Gaussian pulse source with a rise time of 45 ps is generated by the time domain module and pulse generating network and fed to the Vivaldi antenna. A digital sampling oscilloscope is utilized to display and measure the back-scattered fields. The overall process for target detection was initially validated using a far field radar system [35], while the current setup is validated for imaging metallic targets [36]. In this research, the setup is used for the breast tumor imaging application. In order to be utilized as a physical, active TR system for rapid clinical investigations, the passive TR experimental system needs to be modified into two modules. The first

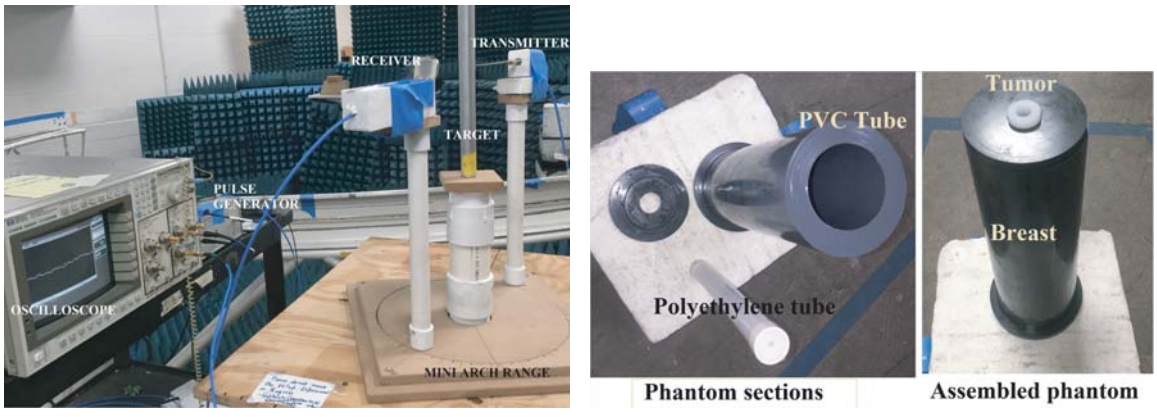

(a) (b)

Figure 10. (a) Time domain experimental system, (b) breast phantom.

module would comprise the transmitter and multiple receiver channels with RF switching circuits for automated scanning. The second module would comprise TR based RF circuits as mentioned before [26], which can calculate the pulse delay and amplitude scaling for each channel, modify and time reverse the received waveforms and feed them as input to individual receiver channels, in order to perform physical time reversal.

4.2. Breast Phantom Design

A chemical liquid based breast phantom is used in this research [37], as shown in Fig. 10(b). A transverse section of the cylindrical phantom with a radius of 8 cm and a height of 30 cm corresponds to a breast coronal region. Soybean oil ($\varepsilon_r = 2.6$, $\sigma = 0.05$ S/m at 6 GHz) is poured in a PVC cylindrical tube ($\varepsilon_r = 3$), representing fatty breast tissues. A 35% dilute diacetin solution ($\varepsilon_r = 8.7$, $\sigma = 1.9$ S/m at 6 GHz) is poured in a polyethylene cylindrical tube ($\varepsilon_r = 2.3$), representing the tumor region. Although the dielectric properties of this phantom fall slightly below the expect dielectric properties of realistic breast tissues, the contrast between malignant and non-malignant tissues (3 : 1) in the phantom is similar to that of actual tissue. The scattered signal from the tumor in the presence of skin is an amplitude scaled and time delayed version of the corresponding scattered signal without the skin, as mentioned in [38]. However, the authors acknowledge that there might be added complexities to the algorithm performance due to the reflection from the breast-skin interface. The effect of the skin layer is not studied as part of the experiments and will be investigated as part of future research. Some of the benefits of the phantom include stability, low cost, ease of disposal and dielectric contrast. The axially-invariant geometry allows a 2D imaging method.

4.3. Experimental Results

The breast phantom was placed on a wooden stand, and the scattered fields were collected at different receiver positions. The scattered data were then fed to the TRI algorithm for studying the imaging and thermal therapy capabilities. The nominal values of the breast tissue simulants were used in the back-propagation simulation.

4.3.1. Single Tumor

In the first case, a tumor simulant of radius 1 cm was placed at the center of the breast. The back-propagation shows the fields originating from the receiver array, focusing at the tumor location and diverging away from it. The TR integrated energy is focused almost ideally around the tumor location, as shown in Fig. 11(a). However, there is a spreading effect observed due to diffraction limited resolution, lack of complete knowledge of tissue heterogeneity and frequency dispersive nature and measurement errors. The contour boundaries along with scale values of the TR SAR image (Fig. 11(b)) shows that most of the energy is absorbed by the tumor region, with approximately 60% more absorption than surrounding tissues. This demonstrates the possibility of using microwave TR for thermal therapy applications.

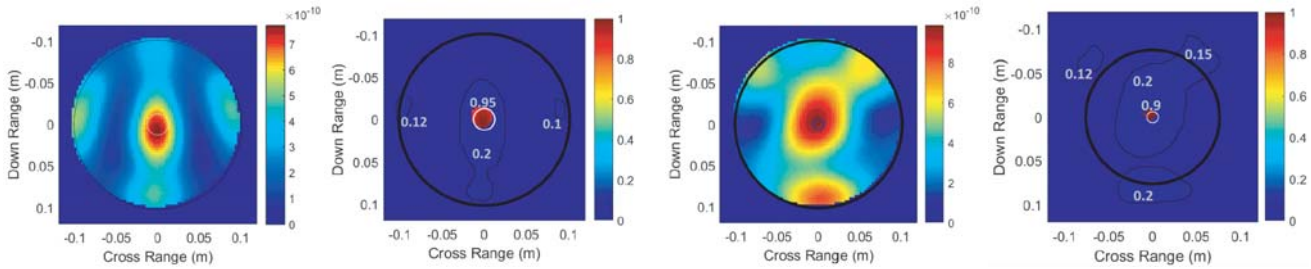

Figure 11. Experimental results for breast phantom with (a), (b) 1 cm tumor and (c), (d) 5 mm tumor. (a) Energy (mE = 3.7), (b) SAR (mSAR = 25), (c) Energy (mE = 2.4), (d) SAR (mSAR = 23).

A similar procedure was followed for a much smaller tumor of radius 5 mm. The TR energy for this case is focused around the tumor, but has a wider spreading effect. Moreover, a significant fraction of the energy is localized at the breast-skin interface as seen in Fig. 11(c). This is a limiting situation for the experiments, and tumors smaller than 5 mm are barely detected by TR. Although the TR SAR image (Fig. 11(d)) again shows considerable energy absorbed by the tumor region with approximately 40% more absorption than the surrounding tissues, a portion of the energy is also absorbed by the skin-breast interface as well as surrounding tissues. Thus higher energy might be required to elevate the temperature of the tumor, which might lead to excessive heating of the surrounding tissues. Careful studies need to be conducted to ensure that the surrounding tissues are not affected.

4.3.2. Multiple Tumors

The capability of the experimental imaging system was also investigated for detection of multiple tumors in the breast region. The two tumor simulants used in the prior cases are placed together in the breast region, with the small tumor placed at the center and the big tumor located closer to the breast wall. The gap between the two tumors is 7 cm, which is approximately 3 times the down-range resolution and 4 times the threshold of tumor spacing, as obtained from Fig. 3(b). The back-propagated integrated energy shows efficient focusing capabilities, with most of the energy focused around the tumor locations, as shown in Fig. 12(a). The spreading effect is still observed due to prior mentioned reasons as well as cross coupling between the tumors. More energy is focused on the larger tumor, because of its larger scattering cross-sectional area. The TR SAR image given by Fig. 12(b) reveals that most of the energy is absorbed by the tumor region with approximately 50% more absorption than the surrounding tissues. However, regions close to the tumor are also heated by significant energy absorption.

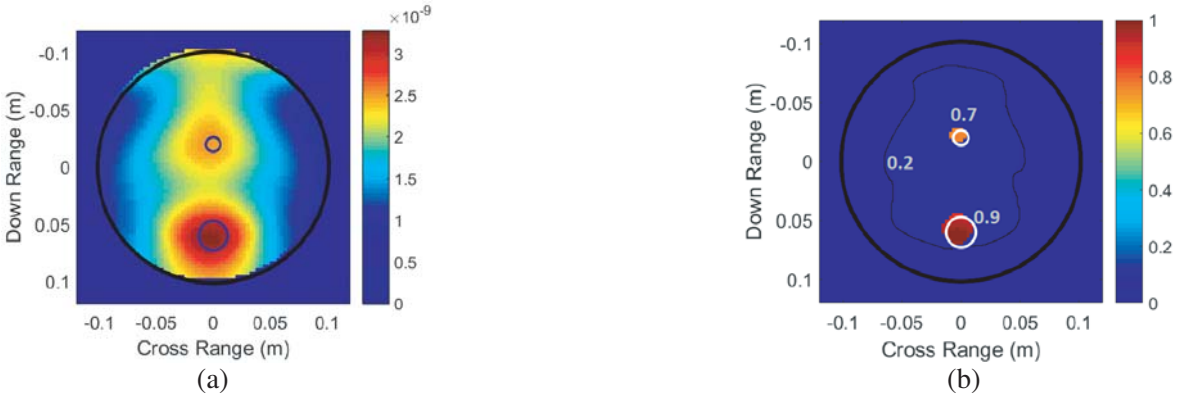

Figure 12. Experimental results for breast phantom with multiple tumors. (a) Energy (mE = 3.8), (b) SAR (mSAR = 20).

5. CONCLUSION AND FUTURE WORK

A microwave TRI system is developed for imaging of breast tumors. The SAR of the time reversed fields describes the absorption rates of the breast tissues for potential thermal therapy applications. Simulations and parametric studies demonstrate the feasibility and evaluate the limits of the algorithm. A measurement system is developed for conducting TRI experiments on breast phantoms with single and closely spaced tumors. The SAR studies reveal much higher absorption rates for tumor tissues than surrounding breast tissues. However, studies need to be performed to evaluate the temperature inside the breast. The initial results shown in this paper are promising and builds the foundation and validates the entire system for potential real time 3D breast imaging applications.

The current computational time is much less than the time required to perform a detailed 3-D image reconstruction of the breast tissue profile. The average measurement time is approximately 5 min, while the back-propagation simulations conducted on an Intel core i7 (4 CPU) processor, 2.6 GHz with 8 GB

RAM, takes approximately 3 min. With a fully automated coherent antenna array experimental setup, coupled with a parallel supercomputer for the back-propagation simulations, this method has potential for real time implementation. Future research includes development of a 3D model based TRI system and performing more practical experiments with 3D breast phantoms with multiple, sub-wavelength sized tumors to investigate the robustness and super resolution capabilities of the proposed microwave TRI system. In order to translate the method from lab into the clinical stage, an algorithm needs to be developed that is capable of extracting tumor contribution from total fields, thus eliminating the need for the healthy breast contribution [20, 39]. Moreover, a detailed tissue model along with clutter removal techniques is needed for validating the approach for further complicated and realistic scenarios [40]. The increase in breast tissue temperature needs to be calculated from the bio heat transfer equation, as well as measured for gelatin based phantoms, in order to determine the potential of the TRI method for thermal therapy applications. Finally, the recent development in the field of cheap and compact RF circuits for TR will be utilized to develop a physical TRI system that can use the similar hardware systems for imaging as well as thermal therapy applications.

ACKNOWLEDGMENT

The authors thank B. Wright for his help with the experimental setup and phantom design.

REFERENCES

1. Fink, M., "Time reversal of ultrasonic fields. I. Basic principles," *IEEE Trans. Ultrason., Ferroelect., Freq. Control*, Vol. 39, No. 5, 555–566, 1992.
2. Lerosey, G., J. De Rosny, A. Tourin, A. Derode, G. Montaldo, and M. Fink, "Time reversal of electromagnetic waves," *Phys. Rev. Lett.*, Vol. 92, No. 19, 193904, 2004.
3. Mukherjee, S., A. Tamburrino, M. Haq, S. Udpa, and L. Udpa, "Far field microwave NDE of composite structures using time reversal mirror," *NDT & E International*, Vol. 93, 7–17, 2018.
4. Tabar, L., A. Gad, L. H. Holmberg, U. Ljungquist, C. J. G. Fagerberg, L. Baldetorp, O. Gröntoft, B. Lundström, J. C. Månson, et al., "Reduction in mortality from breast cancer after mass screening with mammography: Randomised trial from the breast cancer screening working group of the swedish national board of health and welfare," *The Lancet*, Vol. 325, No. 8433, 829–832, 1985.
5. Mettler, F. A., A. C. Upton, C. A. Kelsey, R. N. Ashby, R. D. Rosenberg, and M. N. Linver, "Benefits versus risks from mammography: A critical reassessment," *Cancer*, Vol. 77, No. 5, 903–909, 1996.
6. Dullum, J. R., E. C. Lewis, and J. A. Mayer, "Rates and correlates of discomfort associated with mammography," *Radiology*, Vol. 214, No. 2, 547–552, 2000.
7. Wust, P., B. Hildebrandt, G. Sreenivasa, B. Rau, J. Gellermann, H. Riess, R. Felix, and P. M. Schlag, "Hyperthermia in combined treatment of cancer," *The Lancet Oncology*, Vol. 3, No. 8, 487–497, 2002.
8. Kowalski, M, B. Behnia, A. G. Webb, and J.-M. Jin, "Optimization of electromagnetic phasedarrays for hyperthermia via magnetic resonance temperature estimation," *IEEE Transactions on Biomedical Engineering*, Vol. 49, No. 11, 1229–1241, 2002.
9. Converse, M., E. J. Bond, S. C. Hagness, and B. D. van Veen, "Ultrawide-band microwave spacetime beamforming for hyperthermia treatment of breast cancer: A computational feasibility study," *IEEE Transactions on Microwave Theory and Techniques*, Vol. 52, No. 8, 1876–1889, 2004.
10. Converse, M., E. J. Bond, B. D. Veen, and C. Hagness, "A computational study of ultra-wideband versus narrowband microwave hyperthermia for breast cancer treatment," *IEEE Transactions on Microwave Theory and Techniques*, Vol. 54, No. 5, 2169–2180, 2006.
11. Bond, E. J., X. Li, S. C. Hagness, and B. D. van Veen, "Microwave imaging via space-time beamforming for early detection of breast cancer," *IEEE Transactions on Antennas and Propagation*, Vol. 51, No. 8, 1690–1705, 2003.

12. Al Shehri, S. A., S. Khatun, A. B. Jantan, R. S. A. Raja Abdullah, R. Mahmud, and Z. Awang, "Experimental breast tumor detection using Nn-based UWB imaging," *Progress In Electromagnetics Research*, Vol. 111, 447–465, 2011.
13. O'Halloran, M., E. Jones, and M. Glavin, "Quasi-multistatic mist beamforming for the early detection of breast cancer," *IEEE Transactions on Biomedical Engineering*, Vol. 57, No. 4, 830–840, 2010.
14. Henty, B. E. and D. D. Stancil, "Multipath-enabled super-resolution for RF and microwave communication using phase-conjugate arrays," *Phys. Rev. Lett.*, Vol. 93, No. 24, 243904, 2004.
15. Yavuz, M. E. and F. L. Teixeira, "Full time-domain dort for ultrawideband electromagnetic fields in dispersive, random inhomogeneous media," *IEEE Transactions on Antennas and Propagation*, Vol. 54, No. 8, 2305–2315, 2006.
16. Akıncı, M. N., M. Çayören, and I. Akduman, "Near-field orthogonality sampling method for microwave imaging: Theory and experimental verification," *IEEE Transactions on Microwave Theory and Techniques*, Vol. 64, No. 8, 2489–2501, 2016.
17. Roy Paladhi, P., A. Sinha, A. Tayebi, L. Udpa, and S. S. Udpa, "Improved backpropagation algorithms by exploiting data redundancy in limited-angle diffraction tomography," *Progress In Electromagnetics Research B*, Vol. 66, 1–13, 2016.
18. Vargas, H. I., W. C. Dooley, R. A. Gardner, K. D. Gonzalez, R. Venegas, S. H. Heywang-Kobrunner, and A. J. Fenn, "Focused microwave phased array thermotherapy for ablation of early-stage breast cancer: Results of thermal dose escalation," *Annals of Surgical Oncology*, Vol. 11, No. 2, 139–146, 2004.
19. Stang, J., M. Haynes, P. Carson, and M. Moghaddam, "A preclinical system prototype for focused microwave thermal therapy of the breast," *IEEE Transactions on Biomedical Engineering*, Vol. 59, No. 9, 2431–2438, 2012.
20. Pettinelli, E., A. Di Matteo, E. Mattei, L. Crocco, F. Soldovieri, J. D. Redman, and A. P. Annan, "GPR response from buried pipes: Measurement on field site and tomographic reconstructions," *IEEE Transactions on Geoscience and Remote Sensing*, Vol. 47, No. 8, 2639–2645, 2009.
21. Thomas, J.-L. and M. A. Fink, "Ultrasonic beam focusing through tissue inhomogeneities with a time reversal mirror: Application to transskull therapy," *IEEE Transactions on Ultrasonics, Ferroelectrics, and Frequency Control*, Vol. 43, No. 6, 1122–1129, 1996.
22. De Rosny, J., G. Lerosey, and M. Fink, "Theory of electromagnetic time-reversal mirrors," *IEEE Transactions on Antennas and Propagation*, Vol. 58, No. 10, 3139–3149, 2010.
23. Yavuz, M. E. and F. L. Teixeira, "Ultrawideband microwave sensing and imaging using time-reversal techniques: A review," *Remote Sensing*, Vol. 1, No. 3, 466–495, 2009.
24. Fink, M., D. Cassereau, A. Derode, C. Prada, P. Roux, M. Tanter, J.-L. Thomas, and F. Wu, "Time-reversed acoustics," *Rep. Prog. Phys.*, Vol. 63, No. 12, 1933, 2000.
25. Leopold, K. A., M. Dewhirst, T. Samulski, J. Harrelson, J. A. Tucker, S. L. George, R. K. Dodge, W. Grant, S. Clegg, L. R. Prosnitz, et al., "Relationships among tumor temperature, treatment time, and histopathological outcome using preoperative hyperthermia with radiation in soft tissue sarcomas," *International Journal of Radiation Oncology Biology Physics*, Vol. 22, No. 5, 989–998, 1992.
26. Zhai, H., S. Sha, V. K. Shenoy, S. Jung, M. Lu, K. Min, S. Lee, and D. S. Ha, "An electronic circuit system for time-reversal of ultra-wideband short impulses based on frequency-domain approach," *IEEE Transactions on Microwave Theory and Techniques*, Vol. 58, No. 1, 74–86, 2010.
27. Yee, K., "Numerical solution of initial boundary value problems involving Maxwell's equations in isotropic media," *IEEE Transactions on Antennas and Propagation*, Vol. 14, No. 3, 302–307, 1966.
28. Klauenberg, B. J. and D. Miklavcic, *Radio Frequency Radiation Dosimetry and Its Relationship to the Biological Effects of Electromagnetic Fields*, Vol. 82, Springer Science & Business Media, 2012.
29. Lazebnik, M., D. Popovic, L. McCartney, C. B. Watkins, M. J. Lindstrom, J. Harter, S. Sewall, T. Ogilvie, A. Magliocco, T. M. Breslin, et al., "A large-scale study of the ultrawideband microwave dielectric properties of normal, benign and malignant breast tissues obtained from cancer surgeries," *Physics in Medicine and Biology*, Vol. 52, No. 20, 6093, 2007.

30. Chaudhary, S. S., R. K. Mishra, A. Swarup, and J. M. Thomas, "Dielectric properties of normal & malignant human breast tissues at radiowave & microwave frequencies," *Indian Journal of Biochemistry & Biophysics*, Vol. 21, No. 1, 76–79, 1984.
31. Prada, C., S. Manneville, D. Spoliansky, and M. Fink, "Decomposition of the time reversal operator: Detection and selective focusing on two scatterers," *The Journal of the Acoustical Society of America*, Vol. 99, No. 4, 2067–2076, 1996.
32. Lynch, S. P., X. Lei, M. Chavez-MacGregor, L. Hsu, F. Meric-Bernstam, T. A. Buchholz, A. Zhang, G. N. Hortobagyi, V. Valero, and A. M. Gonzalez-Angulo, "Multifocality and multicentricity in breast cancer and survival outcomes," *Annals of Oncology*, Vol. 23, No. 12, 3063–3069, 2012.
33. Esserman, L. J., D. Wolverton, and N. Hylton, "Integration of breast imaging into cancer management," *Current Oncology Reports*, Vol. 2, No. 6, 572–581, 2000.
34. Mukherjee, S., A. Tamburrino, L. Udpa, and S. Udpa, "Nde of composite structures using microwave time reversal imaging," *42nd Annual Review of Progress in Quantitative Nondestructive Evaluation*, Vol. 1706, 100002, AIP Publishing, 2016.
35. Mukherjee, S., L. Udpa, S. Udpa, and E. J. Rothwell, "Target localization using microwave time-reversal mirror in reflection mode," *IEEE Transactions on Antennas and Propagation*, Vol. 65, No. 2, 820–828, 2017.
36. Mukherjee, S., L. Udpa, Y. Deng, P. Chahal, and E. J. Rothwell, "Design of a microwave time reversal mirror for imaging applications," *Progress In Electromagnetics Research C*, Vol. 77, 155–165, 2017.
37. Lazebnik, M., E. L. Madsen, G. R. Frank, and S. C. Hagness, "Tissue-mimicking phantom materials for narrowband and ultrawideband microwave applications," *Physics in Medicine and Biology*, Vol. 50, No. 18, 4245, 2005.
38. Kosmas, P. and C. M. Rappaport, "Time reversal with the FDTD method for microwave breast cancer detection," *IEEE Transactions on Microwave Theory and Techniques*, Vol. 53, No. 7, 2317–2323, July 2005.
39. Klemm, M., I. J. Craddock, J. A. Leendertz, A. Preece, and R. Benjamin, "Radar-based breast cancer detection using a hemispherical antenna array experimental results," *IEEE Transactions on Antennas and Propagation*, Vol. 57, No. 6, 1692–1704, 2009.
40. Zhurbenko, V., "Challenges in the design of microwave imaging systems for breast cancer detection," *Advances in Electrical and Computer Engineering*, Vol. 11, No. 1, 91–96, 2011.